Switched Capacitor-Based PWM- and Phase-Shift-Controlled Multiport Converter with Differential Power Processing Capability for Standalone Photovoltaic Systems Under Partial Shading

Masatoshi Uno, *Member*, *IEEE*, Ryuichi Igarashi, and Yusuke Sato

***Abstract*—Photovoltaic (PV) systems consist of multiple dc-dc converters, such as a front-end converter for a PV panel and a bidirectional converter for battery regulation. In addition, a differential power processing (DPP) converter is desirably installed to preclude partial shading issues of the significant reduction in energy yield and the occurrence of multiple maximum power points. This paper proposes a novel multiport converter (MPC) based on a switched capacitor converter (SCC) with DPP capability to simplify such PV systems by reducing the converter count. The proposed SCC-MPC is derived from the integration of a noninverting PWM buck-boost converter, SCC, and phase-shift (PS) SCC with sharing switches. In addition to the reduced converter count, the proposed MPC achieves reduced circuit volume thanks to the SCC and PS-SCC, both of which are a high power-density converter. The proposed SCC-MPC can regulate the load and battery by PS and PWM controls, respectively, while automatically precluding the partial-shading issues by its DPP capability. The experimental verification using a 200-W prototype demonstrated the load and battery could be independently regulated with preventing the partial shading issues.**

***Keywords*—Differential power processing (DPP) converter, multiport converter (MPC), switched capacitor converter (SCC), phase-shift converter (PS-SCC).**

I. Introduction

Photovoltaic (PV) systems containing a rechargeable battery require multiple dc–dc converters to individually regulate PV panels and battery. A front-end dc-dc converter performs maximum power point tracking (MPPT) for PV panels while a bidirectional dc–dc converter plays a role of battery charge-discharge regulation to allow flexible operation of the PV systems under fluctuating irradiation conditions or even at night.

In general, ordinary standard PV panels consist of three substrings connected in series. Substring characteristics are mismatched by partial shading on PV panels. Partially-shaded substrings, or weak substrings, are less capable of generating current and, therefore, are bypassed by parallel-connected bypass diodes, as shown in Fig. 1(a). Bypassed substrings no longer contribute to power generation, resulting in a significant reduction in power generation of a panel as a whole—partial shading with 10% equivalent area of a panel reportedly results in 30% reduction in energy yield [1]. In addition, the mismatched substring characteristics generate local power point maxima on *P*–*V* characteristics of a panel, as shown in Fig. 1(b). The existence of multiple maximum power points (MPPs)

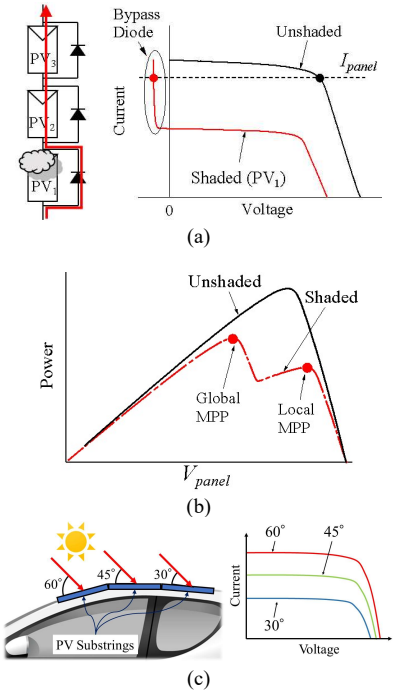

Fig. 1. (a) Substring characteristic mismatch due to partial shading. (b) Panel characteristics with/without partial shading. (c) Substring characteristic mismatch due to uneven irradiance on solar roofs.

This paper is an extension of a conference paper entitled "Switched capacitor converter-based PWM plus phase-shift control multiport converter with differential power processing capability for photovoltaic systems" at *IEEE Int. Conf. Power Electron. (ICPE)*, *ECCE-Asia*, Busan, Korea, May 27−30, 2019.

M. uno and R. Igarashi are with the Graduate School of Science and Engineering, Ibaraki University, Hitachi 316-8511, Japan (e-mail: masatoshi.uno.ee@vc.ibaraki.ac.jp).

Y. Sato is with Panasonic Corporation, Yokohama, 224-8520 Japan (e-mail: sato.yusuke004@jp.panasonic.com).

might hinder and confuse ordinary MPP tracking (MPPT) algorithms to track a global MPP. Similar mismatch situations happen in curved solar panels, such as solar roofs of electric vehicles, because of uneven irradiance on the curved surface, as illustrated in Fig. 1(c) [2].

Differential power processing (DPP) converters, also known as voltage equalizers, are gaining significant attention as a powerful solution to partial shading issues [2]–[20]. High-irradiance substrings transfer power to low-irradiance ones through DPP converters to unify substring voltages or even operate all substrings at each MPP. Since DPP converters process only differential power between high- and low-irradiance substrings, the converter power rating can be rather lower than that of traditional full power processing converters. Applications of DPP converters are not limited to PV systems. Data centers using series-stacked processors necessitate DPP converters to ensure processor voltages remain within the design limit [21].

DPP converters are categorized into several groups based on power redistribution scenarios. Nonisolated bidirectional converters [3]–[7], single-input–multi-output converters [8]–[11], and isolated bidirectional converters [12]–[15] can be used as DPP converters. Among various kinds of DPP converter topologies is a switched capacitor converter (SCC) [16]–[21]. The most prominent feature of SCC-based DPP converters is an enhanced power density or decreased circuit volume in comparison with inductor-based topologies. The energy density of discrete capacitors is reportedly within a range of more than three orders of magnitude over that of similarly scaled inductors [22], [23].

A conventional standalone PV system containing a rechargeable battery and DPP converter is illustrated in Fig. 2(a). In addition to the PV panel and battery, this system requires a unidirectional converter for MPPT, a bidirectional converter for charge-discharge regulation of the battery, and a DPP converter to preclude partial-shading issues of the PV panel. This PV system is prone to be complex and costly as three separate converters are necessary.

To cope with this issue, various kinds of multiport converters (MPCs) that integrate multiple converters into a single unit have been proposed. MPCs are roughly divided into three categories: isolated [24]–[26], partially-isolated [27]–[35], and nonisolated MPCs [36]–[44]. Nonisolated MPCs are the best suitable topology for nonisolated applications because of the lack of bulky, lossy transformers. Although a variety of nonisolated MPC topologies have been proposed for nonisolated standalone PV systems, conventional MPCs integrate only a unidirectional converter for PV panels and bidirectional converter for batteries. In other words, DPP converters remain unintegrated, suggesting there is still room for further integration and simplification.

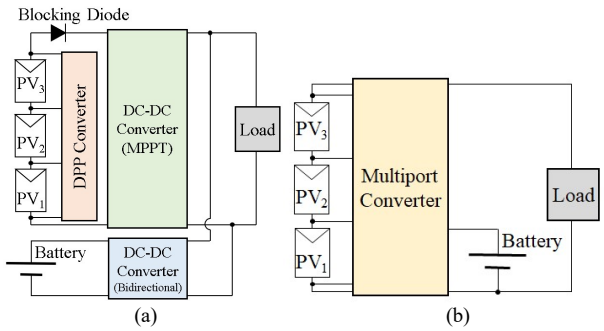

Fig. 2. (a) Conventional PV system with separate converters. (b) Proposed multiport converter system.

Meanwhile, several converters and inverters with DPP capability have also been proposed in our previous works [45]–[48]. These conventional topologies, however, integrate a unidirectional converter and DPP converter into a single unit, whereas bidirectional converters for rechargeable batteries were outside the scope of previous research.

To further simplify nonisolated PV systems, a novel SCC-based MPC integrating the three converters into a single unit has been proposed in our previous study [49]. The schematic diagram of the proposed MPC is depicted in Fig. 2(b). In addition to unidirectional and bidirectional converters, a DPP converter is also integrated. Furthermore, since the proposed MPC is based on the SCC, circuit miniaturization is also feasible. This paper presents the fully developed work of [49].

The rest of this paper is organized as follows. Section II presents the proposed SCC-MPC and its major features. Section III discusses three operation scenarios of MPCs, which are determined by power balance among three input/output ports. Section IV presents the detailed operation analysis and mathematical modeling for the proposed SCC-MPC. Section V discusses a design example of a 200-W prototype. The control system for the proposed MPC is presented in Section VI. The experimental results of a 200-W prototype will be shown in Section VII. The proposed SCC-MPC will be compared with conventional MPCs from various aspects in Section VIII.

II. Proposed SCC-MPC

A. Key Elements for Proposed SCC-Based MPC

The proposed MPC is derived from the combination of three converters shown in Fig. 3: the SCC, phase-shift (PS) SCC, and noninverting PWM buck-boost converter.

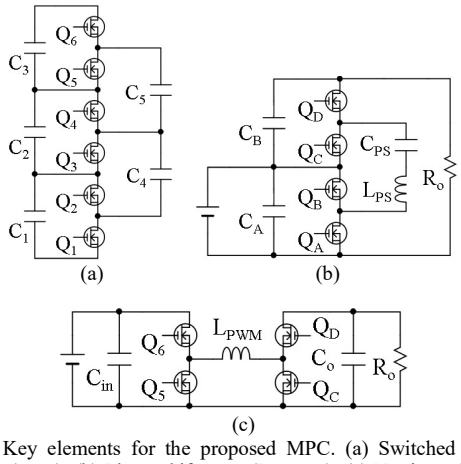

Fig. 3. Key elements for the proposed MPC. (a) Switched capacitor converter (SCC). (b) Phase-shift SCC (PS-SCC). (c) Noninverting PWM buck-boost converter.

The SCC, shown in Fig. 3(a), consists only of switches and capacitors, and its power density can be rather higher than ordinary inductor-based converters thanks to the lack of bulky magnetic components [22], [23]. All capacitor voltages automatically unify at any duty cycles without feedback control, and therefore, the SCC behaves as a voltage equalizer. The SCCs have been used as not only DPP converters for PV panels [16]–[20] but also voltage equalizers for series-connected energy storage cells [50]–[52].

The PS-SCC, shown in Fig. 3(b), is an extended version of an ordinary SCC. The inductor L_{PS} is added to realize PS-based power regulation capability. The amount and direction of power transfer can be controlled by manipulating PS angle φ between a leading and lagging leg [53]. The PS-SCC is driven with a fixed 50% duty cycle and is used to regulate the load voltage V_{out} in the proposed MPC. Although PS-SCCs tend to be slightly bulkier than ordinary SCCs due to the added inductor, their circuit volume would be still considerably small because energy densities of discrete capacitors are in the range of more than three orders of magnitude over similarly scalded inductors [22], [23].

The noninverting PWM buck-boost converter, shown in Fig. 3(c), contains two switching legs and one inductor. The buck-boost converter operates in either buck, boost, or buck-boost mode, depending on driving methods. In the proposed MPC, the buck-boost converter operates in the buck-boost mode, where gating signals for Q_6 and Q_C (or Q_5 and Q_D) synchronize.

B. Derivation of Proposed SCC-MPC

The proposed MPC is derived from integrating these three converters with sharing switches, as shown in Fig. 4. The SCC and PWM buck-boost converter are integrated with sharing switches Q_5 and Q_6. Q_C and Q_D are shared by the PWM buck-boost converter and PS-SCC.

PV substrings PV_1–PV_3 are connected in parallel with capacitors C_1–C_3 in the SCC. All capacitor voltages, as well as substring voltages V_1–V_3, are automatically unified by the SCC, hence precluding the negative influences of partial shading.

The series connection of C_A and C_B is tied to the load. The rechargeable battery is connected to C_A in the PS-SCC, and the voltage of C_A is always equal to the battery voltage V_{bat}. Meanwhile, the voltage of C_B, V_{CB}, can be regulated with the PS control that adjusts the power transfer between C_A and C_B by manipulating the PS angle φ between Q_A–Q_B and Q_C–Q_D.

The input and output ports of the noninverting PWM buck-boost converter correspond to C_3 (or PV_3) and C_B, respectively, and therefore, either V_3 or V_{CB} can be regulated by the PWM control. A diode D is inserted in series with L_{PWM} to prevent the reverse power flow from the battery to the PV panel when the panel generates no power (e.g., at night). This added D plays the role of a blocking diode in conventional systems [see Fig. 2(a)].

Since both the PS-SCC and PWM buck-boost converter contain C_B, V_{CB} ($= V_{out} - V_{bat}$) can be regulated by either PWM or PS control. In general, the load voltage V_{out} must be regulated all the time, whereas a PV panel is periodically unavailable. The PWM buck-boost converter is connected to the PV panel and therefore is periodically disabled when the panel is unavailable. The PS-SCC, on the other hand, is always active because it is connected to the load and battery. Hence, the PS-SCC with PS control should be assigned to seamlessly regulate V_{out}, while the buck-boost converter with PWM control is used to perform PV panel regulation (i.e., MPPT control) or battery charging regulation.

The duty cycle of the PS-SCC ($d_{PS,SCC}$) is fixed to be 50%, with which the amount of power transfer by the PS-SCC can be maximized. The duty cycle of the SCC (d_{SCC}), on the other hand, is manipulated for PWM control. In other words, the duty cycle of the right-hand leg of the PWM buck-boost converter is fixed to be 50%, while that of the left-hand leg is variable.

The concept of the proposed SCC-MPC can be extended by integrating three converters at other switching nodes. The inductor L_{PWM} in Fig. 4 is connected to the switching node c of the SCC and the switching node B of the PS-SCC. Other topologies of the proposed SCC-MPC can be derived by connecting L_{PWM} to other switching nodes, as exemplified in Fig. 5, in which L_{PWM} is connected to the node b and node A. Depending on the switching nodes connected to L_{PWM}, an attainable range of the voltage conversion ratio of V_{out}/V_{PV} can be changed—the SCC-MPC in Fig. 5 achieves a higher voltage conversion ratio of V_{out}/V_{PV} in comparison with the topology of Fig. 4. Hence, the switching nodes for L_{PWM} should be properly selected with considering required conversion ranges. In the following sections, the SCC-MPC in Fig. 4 will be analyzed and demonstrated.

C. Major Features

Although various kinds of nonisolated MPCs have been proposed in previous works, conventional MPCs integrate only two converters for a PV panel and battery [36]–[44]. The proposed MPC, on the other hand, integrates the DPP converter as well, further simplifying the system by reducing the converter count.

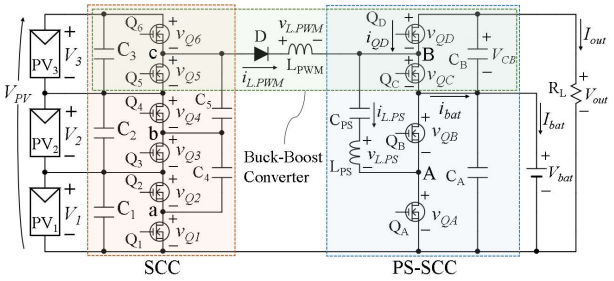

Fig. 4. Proposed SCC-MPC with DPP capability.

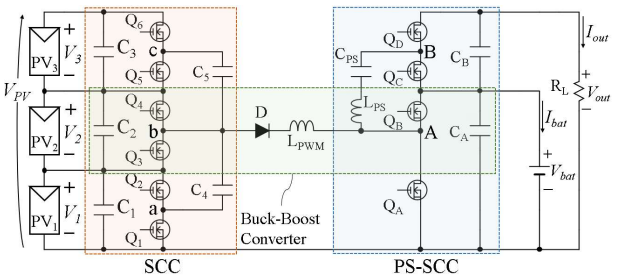

Fig. 5. Other version of proposed SCC-MPC with DPP capability.

Three converters are integrated into a single unit with sharing switches. Hence, in comparison with the case of three separate converters, the total switch count can be reduced from 14 to 10 (see Figs. 3 and 4), achieving the circuit-level simplification—the diode D added in series with L_{PWM} is not included in the total switch count for the fair comparison because it corresponds to the conventional system's blocking diode [see Fig. 2(a)].

The reduced circuit volume is a prominent advantage over conventional MPCs. The SCC and PS-SCC, both of which are a high power-density converter, are used as the foundation of the proposed MPC. In addition, since an applied voltage across L_{PWM} in the buck-boost converter can also be reduced thanks to the SCC and PS-SCC, L_{PWM} can be designed rather smaller than that in the traditional noninverting PWM buck-boost converter.

The previous work proposed an MPC consisting of the PS-SCC and bidirectional PWM converter [44]. Although this MPC employs the PS-SCC as a foundation circuit, the inductor volume of the PWM converter cannot be reduced because the converter integration does not reduce the applied voltage across the inductor. Furthermore, the integration of DPP converters is outside the scope in [44]. Other works reported converters integrating DPP converters or cell equalizers for batteries [45]–[48]. DPP converters and cell equalizers in these topologies are based on a voltage multiplier driven by a transformer, but the transformer's existence hinders circuit miniaturization. The proposed SCC-MPC, on the other hand, not only does not require a bulky transformer but also can reduce the volume of L_{PWM}, rendering itself suitable for circuit miniaturization.

Although three converters are integrated into a single unit, the proposed SCC-MPC requires more switches than do conventional MPCs because, in general, SCC circuits need numerous switches, as can be seen in Fig. 3. The circuit complexity and cost are prone to soar as every two switches require a gate driver circuit consisting of a gate driver IC and auxiliary power supply. Given the advantages and drawbacks, the proposed SCC-MPC is considered best suitable for applications where circuit miniaturization is of great importance (e.g., solar roofs in electric vehicles, satellite power systems, etc.).

Another drawback is a restricted operational range in comparison with the conventional PV systems using separate converters [see Fig. 2(a)]. Since some switches in the SCC-MPC are shared (see Figs. 4 and 5), the operational range is narrower than that of the conventional system. However, the restricted operational range is a common issue to existing MPCs because most MPCs also share switches in the course of integrating converters into a single unit.

III. Operation Scenario

Depending on the power balance among the PV panel, battery, and load, the proposed SCC-MPC operates in either of three scenarios: the single-input dual-output (SIDO) mode, MPPT mode, and single-input single-output (SISO) mode, as illustrated in Fig. 6.

The power balance among three ports is given by

$$P_{PV} = P_{out} + P_{bat} \quad (1)$$

where P_{PV} is the generated power of the panel, P_{out} is the load power, and P_{bat} is the battery charging power. This simple equation suggests a very important fact that controlling two out of three ports determines the remaining one. As briefly mentioned in Section II-B, P_{out} is always regulated by PS control, while PWM control is allocated to regulate either P_{PV} or P_{bat}, depending on operation scenarios.

A. Single-Input Dual-Output (SIDO) Mode

As shown in Fig. 6(a), the PV panel is capable of providing the entire load power P_{out}. The difference between P_{out} and the maximum power of the panel, P_{MP}, is greater than the acceptable maximum charging power (i.e., $P_{MP} > P_{out} + P_{bat}$). Hence, the battery charging power is regulated by the constant-current−constant-voltage (CC−CV) battery charging scheme to prevent excessive charging power.

In this scenario, P_{out} (or V_{out}) is regulated by the PS control, while V_{bat} or the battery current I_{bat} is regulated by PWM control. The PV panel port is unregulated, and the operating voltage of the panel, V_{PV}, is passively determined so that the power balance obeys (1).

B. MPPT Mode

The MPP of the PV panel is tracked by the MPPT control, as shown in Fig. 6(b). The battery is charged or discharged depending on the power balance between P_{PV} and P_{out}. If $P_{MP} > P_{out}$, the surplus power is allocated for battery charging, P_{Bat}. In the case of $P_{MP} < P_{out}$, on the other hand, the battery supports the load by supplying $P_{out} - P_{MP}$.

Similar to the SIDO mode, P_{out} is regulated by PS control. Meanwhile, V_{PV} is regulated to perform the MPPT control, and the battery buffers the surplus or deficit power, depending on the power balance between P_{out} and P_{MP}. In other words, the

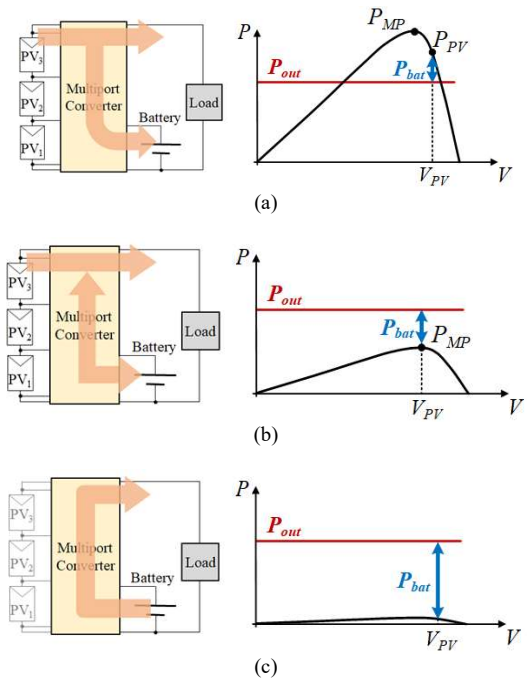

Fig. 6. Power flows in (a) single-input dual-output (SIDO) mode, (b) MPPT mode, and (c) single-input single-output (SISO) mode.

battery port is unregulated in this scenario.

C. Single-Input Single-Output (SISO) Mode

As shown in Fig. 6(c), the PV panel generates no power (e.g., at night), and the battery supplies the entire load power (i.e., $P_{out} = -P_{Bat}$). V_{out} is regulated by PS control, similar to the other two modes. The diode D (see Fig. 4) blocks the current flowing back to the SCC and PV panel.

IV. Operation Analysis

As discussed in the previous section, there are three operation scenarios. This section presents the detailed operation analysis for the SIDO mode only to save page length, but other operation scenarios can be analyzed similarly. All circuit elements are assumed ideal unless otherwise noted. A forward voltage drop of the diode D is ignored. All substring voltages are assumed to be unified by the SCC-based DPP converter.

A. Operation Modes in SIDO Mode

Theoretical operation waveforms and current flow directions are shown in Figs. 7 and 8, respectively. The duty cycle of low-side switches in the PS-SCC ($d_{PS.SCC}$), or the right-hand leg of the PWM buck-boost converter, is fixed to be 50%, whereas that of the SCC (d_{SCC}), or the left-hand leg of the buck-boost converter, is manipulated for PWM control. The analysis is performed on the premise that $V_{PV} > V_{out}$, and all substring voltages V_1–V_3 are perfectly equalized by the SCC as $V_1 = V_2 = V_3 = V_{PV}/3$.

Before detailing individual operation modes, an average voltage of C_{PS}, $V_{C.PS}$, is derived first. Average voltages at the switching nodes of Q_A–Q_B and Q_C–Q_D are $V_{bat}/2$ and $V_{CB}/2 + V_{bat}$, respectively, because of $d_{PS.SCC} = 0.5$. An average voltage of the inductor L_{PS} must be zero under steady-state conditions, and therefore,

$$V_{C.PS} = \frac{V_{CB}}{2} + V_{bat} - \frac{V_{bat}}{2} = \frac{V_{out}}{2} \tag{2}$$

Mode 1 ($T_0 < t \le T_1$) [Fig. 8(a)]: The low-side or odd-numbered switches in the SCC are conducting. C_4 and C_5 are connected in parallel with C_1 and C_2, respectively, and voltages of parallel-connected capacitors become the same. Meanwhile, Q_A and Q_D in the PS-SCC are conducting. The voltage across L_{PWM}, $v_{L.PWM}$, is

$$v_{L.PWM} = \frac{2}{3}V_{PV} - V_{out} \tag{3}$$

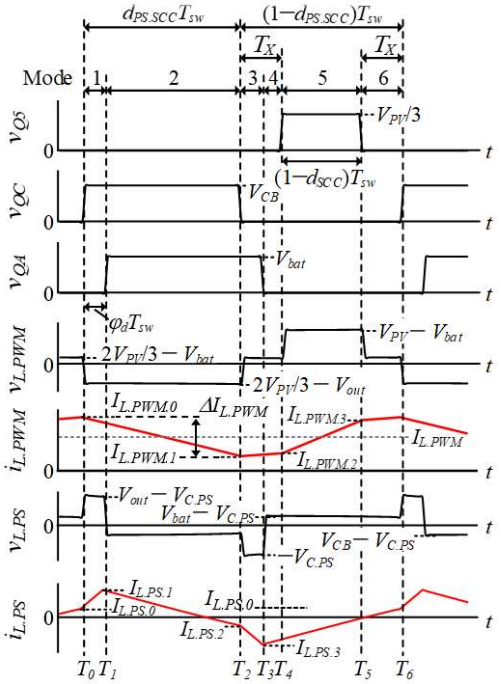

Fig. 7. Key operation waveforms in SIDO mode ($d_{SCC} \ge 0.5$).

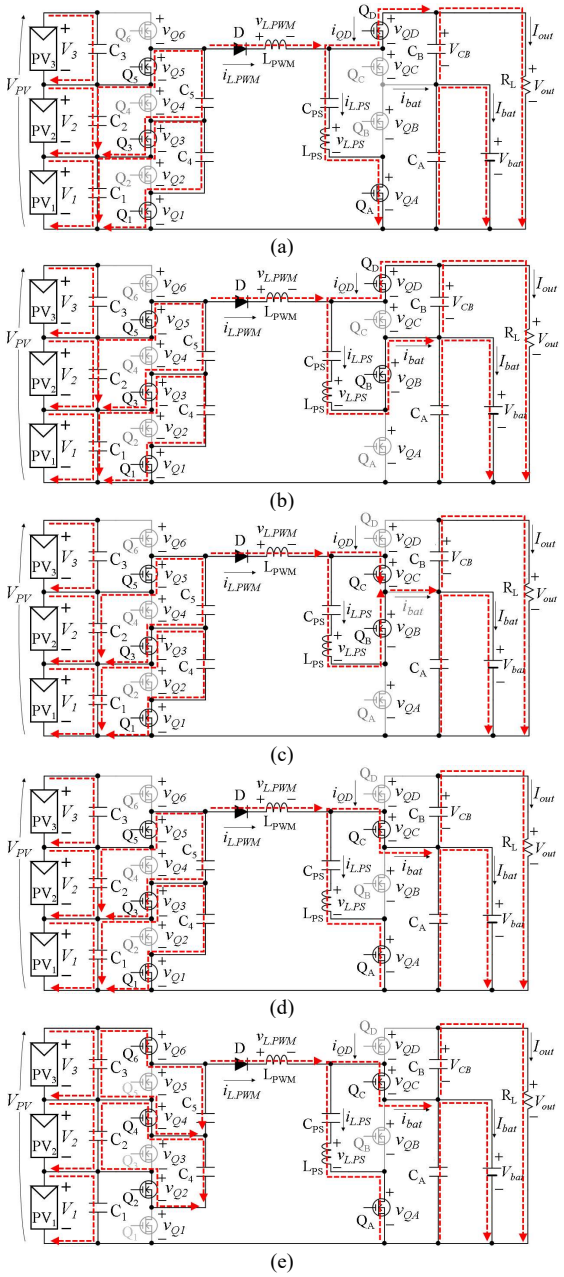

Fig. 8. Current flow directions in SIDO mode. (a) Mode 1, (b) Modes 2, (c) Mode 3, (d) Modes 4 and 6, and (e) Mode 5.

$i_{L.PWM}$ linearly decreases as the polarity of $v_{L.PWM}$ is negative.

The LC tank consisting of C_{PS} and L_{PS} in the PS-SCC is charged by V_{out} as its current $i_{L.PS}$ linearly increases, as

$$i_{L.PS}(t) = I_{L.PS.0} + \frac{V_{out} - V_{C.PS}}{L_{PS}} t = I_{L.PS.0} + \frac{V_{out}}{2L_{PS}} t \quad (4)$$

where $I_{L.PS.0}$ is the initial current of $i_{L.PS}$ at the beginning of this mode [i.e., $I_{L.PS.0} = i_{L.PS}(T_0)$], as designated in Fig. 7.

Mode 2 ($T_1 < t \le T_2$) [Fig. 8(b)]: This mode begins as Q_A and Q_B in the PS-SCC are turned off and on, respectively. The operations of the buck-boost converter and the SCC in this mode are identical to those in Mode 1, and hence, $v_{L.PWM}$ in this mode is identical to that in Mode 1.

The LC tank is charged by C_B. $i_{L.PS}$ is given by

$$\begin{aligned} i_{L.PS}(t) &= I_{L.PS.1} + \frac{V_{CB} - V_{C.PS}}{L_{PS}} (t - T_1) \\ &= I_{L.PS.1} + \frac{V_{out} - 2V_{bat}}{2L_{PS}} (t - T_1) \end{aligned} \quad (5)$$

where $I_{L.PS.1} = i_{L.PS}(T_1)$.

Mode 3 ($T_2 < t \le T_3$) [Fig. 8(c)]: Switching states in the SCC are still identical to those in Mode 1, while Q_C and Q_D in the PS-SCC are turned on and off, respectively. Since L_{PWM} is connected to the battery in this mode, $v_{L.PWM}$ is

$$v_{L.PWM} = \frac{2}{3} V_{PV} - V_{bat} \quad (6)$$

The LC tank is short-circuited through Q_B and Q_C, and $i_{L.PS}$ steeply decreases, as

$$\begin{aligned} i_{L.PS}(t) &= I_{L.PS.2} + \frac{-V_{C.PS}}{L_{PS}} (t - T_2) \\ &= I_{L.PS.2} + \frac{-V_{out}}{2L_{PS}} (t - T_2) \end{aligned} \quad (7)$$

where $I_{L.PS.2} = i_{L.PS}(T_2)$.

Mode 4 ($T_3 < t \le T_4$) [Fig. 8(d)]: Q_A and Q_B in the PS-SCC are turned on and off, respectively. $v_{L.PWM}$ in this mode is the same as that in Mode 3, whereas the LC tank is connected in parallel with the battery. $i_{L.PS}$ is given by

$$\begin{aligned} i_{L.PS}(t) &= I_{L.PS.3} + \frac{V_{bat} - V_{C.PS}}{L_{PS}} (t - T_5) \\ &= I_{L.PS.3} + \frac{2V_{bat} - V_{out}}{2L_{PS}} (t - T_3) \end{aligned} \quad (8)$$

where $I_{L.PS.3} = i_{L.PS}(T_3)$. The switching states of the PS-SCC are unchanged until the end of Mode 6.

Mode 5 ($T_4 < t \le T_5$) [Fig. 8(e)]: All the high-side or even-numbered switches in the SCC are turned on. C_4 and C_5 are connected in parallel with C_2 and C_3, respectively, and parallel-connected capacitor voltages naturally become uniform. Meanwhile, the switching states in the PS-SCC in this mode are identical to those in Mode 4. $v_{L.PWM}$ is given by

$$v_{L.PWM} = V_{PV} - V_{bat} \quad (9)$$

Since $V_{PV} > V_{bat}$, $i_{L.PWM}$ increases.

Mode 6 ($T_5 < t \le T_6$) [Fig. 8(d)]: The low-side switches in the SCC are turned on. The switching states in both the SCC and PS-SCC are identical to those in Mode 4. Hence, $v_{L.PWM}$ and $i_{L.PS}(t)$ in this mode are also identical to those in Mode 4 [see (6) and (8)]. At the end of this mode, $i_{L.PS}(T_6) = I_{L.PS.0}$.

In summary, all capacitors in the SCC are virtually connected in parallel due to the switching operations, and hence, all capacitor voltages as well as voltages V_1–V_3 are unified even under partial shading conditions.

B. Voltage Conversion Ratio of PWM Buck-Boost Converter

From (3), (6), and (9), $v_{L.PWM}$ can be summarized as

$$v_{L.PWM} = \begin{cases} \frac{2}{3} V_{PV} - V_{out} & (Mode\ 1, 2) \\ \frac{2}{3} V_{PV} - V_{bat} & (Mode\ 3, 4, 6) \\ V_{PV} - V_{bat} & (Mode\ 5) \end{cases} \quad (10)$$

The length of Mode 3–4 is equal to that of Mode 6, both of which are defined as T_X (as designated in Fig. 7). Since $d_{PS.SCC} = 0.5$, T_X is expressed as

$$\begin{aligned} T_X &= \frac{(1 - d_{PS.SCC}) - (1 - d_{SCC})}{2} T_{sw} \\ &= \frac{d_{SCC} - d_{PS.SCC}}{2} T_{sw} = \frac{d_{SCC} - 0.5}{2} T_{sw} \end{aligned} \quad (11)$$

where T_{sw} is the switching period.

The output voltage V_{out} can be yielded the volt-sec balance on L_{PWM}, as

$$V_{out} = \frac{2}{3} (3 - d_{SCC}) V_{PV} - V_{bat} \quad (12)$$

This equation suggests that V_{PV} and V_{bat} are duty-dependent and are PWM-controllable if V_{out} is a fixed constant value.

C. Inductor Ripple Current of Buck-Boost Converter

The inductor ripple current of the PWM buck-boost converter in the proposed MPC is yielded and compared with that of the traditional noninverting buck-boost converter [see Fig. 3(c)] in this subsection. As discussed in the previous subsection, $d_{PS.SCC}$ is fixed to be 0.5 while d_{SCC} is manipulated to regulate V_{out}. Hence, mathematical expressions of the ripple current differ depending on whether $d_{SCC} \ge 0.5$.

The inductor ripple current $\Delta I_{L.PWM}$ in the case of $d_{SCC} \ge 0.5$ is yielded from Modes 1 and 2 (see Fig. 7), as

$$\begin{aligned} \Delta I_{L.PWM} &= \frac{\left| \frac{2}{3} V_{PV} - V_{out} \right|}{L_{PWM}} d_{PS.SCC} T_{sw} \\ &= \frac{\left| \frac{2}{3} V_{PV} - V_{out} \right| T_{sw}}{2L_{PWM}} \end{aligned} \quad (13)$$

Meanwhile, operation waveforms of the PWM buck-boost converter in the case of $d_{SCC} < 0.5$ are shown in Fig. 9—the operation is divided into Modes A–C, and waveforms related to PS-SCC (i.e., v_{QA}, $v_{L.PS}$, and $i_{L.PS}$) are excluded because $\Delta I_{L.PWM}$ is independent on these functions. $\Delta I_{L.PWM}$ in the case of $d_{SCC} < 0.5$ is yielded from Mode C, as

$$\begin{aligned} \Delta I_{L.PWM} &= \frac{|V_{PV} - V_{bat}|}{L_{PWM}} (1 - d_{PS.SCC}) T_{sw} \\ &= \frac{|V_{PV} - V_{bat}| T_{sw}}{2L_{PWM}} \end{aligned} \quad (14)$$

Substituting (12) into (13) and (14) produces

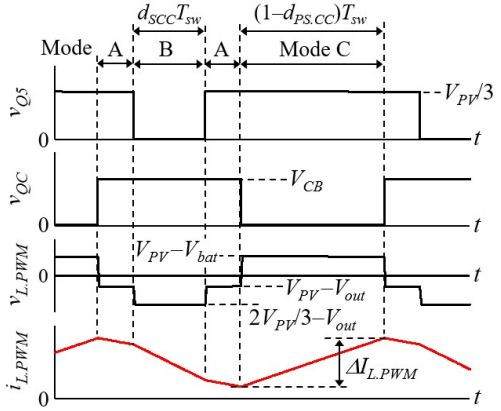

Fig. 9. Key operation waveforms of PWM buck-boost converter in the proposed SCC-MPC (d_{SCC} < 0.5).

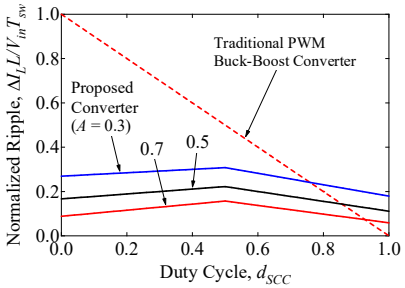

Fig. 10. Normalized inductor ripple current of PWM buck-boost converters.

$$\Delta I_{L.PWM} = \begin{cases} \dfrac{|2d_{SCC} - 4 + 2A|V_{PV}T_{sw}}{6(1+A)L_{PWM}} & (d_{SCC} \geq 0.5) \\ \dfrac{(2d_{SCC}A + 3 - 3A)V_{PV}T_{sw}}{6(1+A)L_{PWM}} & (d_{SCC} < 0.5) \end{cases} \quad (15)$$

where $A = V_{bat}/V_{out}$.

$\Delta I_{L.PWM}$ is normalized by $V_{PV}T_{sw}/L_{PWM}$ and is compared with that of the ordinary noninverting PWM buck-converter [Fig. 3(c)] at the same normalized condition, as shown in Fig. 10—the duty cycle of Q_5 in Fig. 3(c) is defined as d_{SCC}. $\Delta I_{L.PWM}$ of the proposed converter varies with A and does not reach zero because of the existence of the battery voltage V_{bat} (= $A \times V_{out}$). However, the proposed converter shows lower $\Delta I_{L.PWM}$ over the wide range of d_{SCC} because the applied voltage across L_{PWM} can be reduced thanks to the integration with the SCC and PS-SCC (see $v_{L.PWM}$ in Figs. 7 and 9). This trend suggests that the inductance as well as the inductor volume for a given ripple current can be reduced. Meanwhile, even if an SCC-based DPP converter and PS-SCC-based bidirectional converter are employed in the conventional PV system [Fig. 2(a)], the inductor volume reduction is not feasible because $\Delta I_{L.PWM}$ is unchanged from that of the traditional PWM buck-boost converter.

D. Modeling for PS-SCC

The battery charging current, I_{bat}, can be modeled by integrating i_{bat} (see Fig. 4). Meanwhile, the load current I_{out} can be modeled by integrating the current of Q_D, i_{QD}, flowing from the source to drain pins. From the operation modes in Fig. 8, i_{bat} and i_{QD} are summarized as

$$i_{bat} = \begin{cases} 0 & (Mode\ 1) \\ i_{L.PS} & (Mode\ 2) \\ I_{L.PWM} & (Mode\ 3) \\ I_{L.PWM} - i_{L.PS} & (Mode\ 4,5,6) \end{cases} \quad (16)$$

$$-i_{QD} = \begin{cases} I_{L.PWM} - i_{L.PS} & (Mode\ 1,2) \\ 0 & (Mode\ 3,4,5,6) \end{cases} \quad (17)$$

where $I_{L.PWM}$ is the average of $i_{L.PWM}$.

The operation of the PS-SCC in Modes 1–2 are symmetric to that in Modes 3–6 because of $d_{PS.SCC}$ = 0.5. The operation symmetry yields the following relationship.

$$\begin{cases} I_{L.PS.0} = -I_{L.PS.2} \\ I_{L.PS.1} = -I_{L.PS.3} \end{cases} \quad (18)$$

From (4), (5), (7), and (8),

$$\begin{cases} I_{L.PS.1} = \dfrac{-V_{out} - 2(2d_\varphi - 1)V_{bat}}{8f_{sw}L_{PS}} \\ I_{L.PS.2} = \dfrac{(4d_\varphi - 1)V_{out} - 2(2d_\varphi - 1)V_{bat}}{8f_{sw}L_{PS}} \end{cases} \quad (19)$$

where d_φ is the phase-shift duty cycle that is defined as

$$d_\varphi = \frac{\varphi}{2\pi} \quad (20)$$

Integrating i_{bat} over a switching period yields I_{bat}, as

$$\begin{aligned} I_{bat} &= \frac{1}{T_{sw}} \int_{T_0}^{T_6} i_{bat} dt \\ &= \frac{V_{out}(1 - |2d_\varphi|)d_\varphi}{4f_{sw}L_{PS}} + \frac{1}{2} I_{L.PWM} \end{aligned} \quad (21)$$

The first term on the right-hand side corresponds to the current delivered by the PS-SCC alone. The second term on the right-hand side represents the current flowing from L_{PWM}. In the case of $I_{L.PWM}$ = 0 in the SISO mode, (21) is rewritten as

$$I_{bat} = \frac{V_{out}(1 - |2d_\varphi|)d_\varphi}{4f_{sw}L_{PS}} \quad (22)$$

This equation is identical to that of the conventional PS-SCC [53].

Similarly, integrating i_{QD} over a switching period T_{sw} yields I_{out}, as

$$\begin{aligned} I_{out} &= \frac{1}{T_{sw}} \int_{T_0}^{T_6} -i_{QD} dt \\ &= -\frac{V_{bat}(1 - |2d_\varphi|)d_\varphi}{4f_s L_{PS}} + \frac{1}{2} I_{L.PWM} \end{aligned} \quad (23)$$

Combining (22) and (23) produces

$$I_{L.PWM} = 2\frac{V_{out}I_{out} + V_{bat}I_{bat}}{V_{out} + V_{bat}} = 2\frac{P_{out} + P_{bat}}{V_{out} + V_{bat}} \quad (24)$$

where P_{out} and P_{bat} are the output power and battery charging power, respectively.

E. SCC

The previous work performed a thorough analysis for the SCCs [56] and revealed that SCCs can be equivalently expressed using an equivalent resistor R_{eq} that is given by

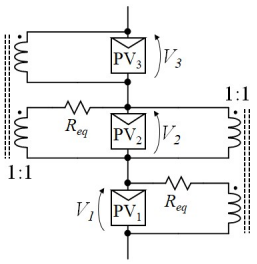

Fig. 11. Equivalent circuit of SCC

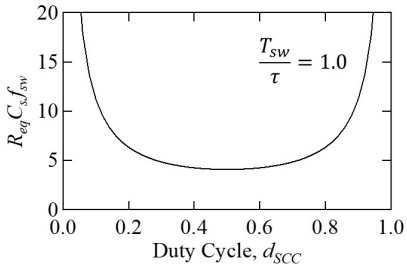

Fig. 12. Normalized R_{eq} as a function of d_{SCC}.

$$R_{eq} = \frac{1}{C_s f_{sw}} \frac{exp\left(\frac{T_{sw}}{\tau}\right) - 1}{\left\{exp\left(\frac{d_{SCC} T_{sw}}{\tau}\right) - 1\right\}\left\{exp\left(\frac{(1 - d_{SCC}) T_{sw}}{\tau}\right) - 1\right\}} \tag{25}$$

where C_s is the series combined capacitance of two capacitors in the SCC (i.e., $C_s = C/2$, where C is the capacitance of each capacitor)—each loop in the SCC contains two capacitors. f_{sw} is the switching frequency, and τ is the time constant formed by C_s and total resistance in a current loop.

The SCC-based DPP converter can reportedly be expressed using a dc equivalent circuit, as shown in Fig. 11 [45]. All substrings are connected in parallel through an ideal transformer and R_{eq}, and therefore, substring voltages are automatically equalized—the lower the value of R_{eq}, the smaller will be the voltage difference among substrings.

Fig. 12 shows R_{eq} normalized by $1/C_s f_{sw}$ as a function of d_{SCC}. R_{eq} increases as d_{SCC} moves away from 0.5. In the range of $0.1 < d_{SCC} < 0.9$, R_{eq} is sufficiently small, and adequate DPP converter performance can be expected. The tendency in Fig. 12 suggests the MPC should not operate with extreme duty cycles to avoid insufficient DPP converter performance.

V. Design Example

This section presents a design example of a 200-W prototype (P_{out} = 100W and P_{bat} = 100 W) for standard 60-cell PV panels comprising three substrings. The target specifications are V_{out} = 28 V, V_{PV} = 28.8 V, V_{bat} = 13.6−16.8 V at f_{sw} = 100 kHz. A short circuit current of the PV panel is 6.0 A. The maximum allowable $|\varphi_d|$ is 0.25.

A. PS-SCC

According to (21), $I_{L.PWM}/2$ contributes to I_{bat} in the SIDO mode. In the SISO mode, on the other hand, I_{bat} does not contain $I_{L.PWM}/2$, as (22) indicates. These equations suggest that the PS-SCC in the proposed MPC processes larger power in the SISO mode than in the SIDO mode. Hence, the LC tank in the PS-SCC should be designed focusing on the SISO mode. To satisfy P_{out} = 100 W at $|d_\varphi| = 0.25$, L_{PS} can be obtained from (21), as

$$\begin{aligned} L_{PS} &= \frac{V_{out} V_{bat}\left(1 - \left|2 d_\varphi\right|\right) d_\varphi}{4 f_{sw} V_{bat} I_{bat}} \\ &= \frac{28\ V \times 13.6\ V (1 - |2 \times 0.25|) 0.25}{4 \times 100\ kHz \times 100\ W} \approx 1.2\ \mu H \end{aligned} \tag{26}$$

The capacitance C_{PS} should be chosen so that the LC tank does not resonate. C_{PS} is determined so that the resonant frequency f_r is lower than one-fifth of f_{sw},

$$\begin{aligned} I_{L.PWM} &= \frac{1}{2\pi\sqrt{L_{PS} C_{PS}}} < \frac{f_{sw}}{5} \\ C_{PS} &= 52.8\ \mu F \rightarrow 66\ \mu F \end{aligned} \tag{27}$$

B. PWM Buck-Boost Converter

In general, an inductor in PWM converters is designed so that a ripple current at a full load is around 30%. However, unlike ordinary PWM converters, the inductor current $I_{L.PWM}$ in the proposed MPC contributes not only to the load current I_{out} but also to the battery current I_{bat}. In this design example, the inductance L_{PWM} is determined to achieve a 30% ripple current at the full output load of P_{out} = 100 W and P_{bat} = 0.

Substituting P_{bat} = 0 into (24) produces

$$\begin{aligned} I_{L.PWM} &= 2\frac{V_{out} I_{out}}{V_{out} + V_{bat}} \\ &= 2\frac{100\ W}{28\ V + 13.6\ V} = 4.81\ A \end{aligned} \tag{28}$$

Substituting $I_{L.PWM}$ = 4.81 A and the ripple factor $\alpha = \Delta I_{L.PWM}/I_{L.PWM}$ = 30% into (13) yields

$$\begin{aligned} L_{PWM} &= \frac{V_{out} - \frac{2}{3} V_{PV}}{\alpha I_{L.PWM}} d_{PS.SCC} T_{sw} \\ &= \frac{28\ \text{V} - \frac{2}{3} 28.8\ \text{V}}{0.3 \times 4.81 \text{A}} 0.5 \times 10\ \mu s = 30.5\ \mu H \rightarrow 33\ \mu H \end{aligned} \tag{29}$$

C. SCC

This subsection determines C_s or C [see (25)] in the SCC by using the dc equivalent circuit of Fig. 11. The previous works reported DPP converters capable of processing 20%–30% of the panel's maximum power can satisfactorily enhance the annual energy yield of partially shaded PV panels [12], [57]. Accordingly, a current equivalent to 30% of the substring's short-circuit current (i.e., 6.0 A×0.3 = 1.8 A) is assumed to flow through the equivalent resistance R_{eq}. The capacitance C_s in (25) is determined so that a voltage drop across R_{eq} is less than 5% of a substring voltage of 9.6 V (= 28.8/3).

$$\begin{aligned} R_{eq}(6.0\ \text{A} \times 0.3) &< 9.6\ \text{V} \times 0.05 \\ \rightarrow R_{eq} &< 0.27\ \Omega \end{aligned} \tag{30}$$

Suppose the total resistance in a current loop of the SCC is 0.02 Ω, which includes ESR of capacitors and on-resistance of switches, C_s is determined to be 50 μF, or C = 100 μF.

VI. Control System

The control block diagram for the proposed SCC-MPC is shown in Fig. 13. $d_{PS.SCC}$ is always fixed to be 50%, while the

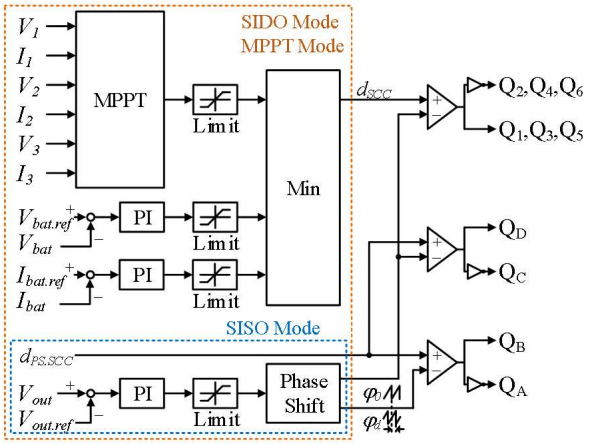

Fig. 13. Control block diagram.

PS duty cycle φ_d is manipulated to regulate V_{out} in all operational scenarios. On the other hand, d_{SCC} is manipulated to regulate either the PV panel or battery, depending on the power balance, as discussed in Section III.

Substring voltages V_1–V_3 and currents I_1–I_3 are measured to calculate the panel power P_{PV} (i.e., $P_{PV} = V_1I_1 + V_2I_2 + V_3I_3$). Any MPPT technique can be used to control the proposed SCC-MPC. In our study, an ordinary hill-climbing MPPT algorithm is employed in the experimental verification tests (Section VII).

The charge current and voltage in the SIDO mode are determined by $I_{bat.ref}$ and $V_{bat.ref}$, respectively. One out of three control objectives (P_{PV}, I_{bat}, and V_{bat}) is selected by the minimum function. The minimum function seamlessly switches the SIDO or MPPT modes to generates d_{SCC}, depending on the power balance.

VII. Experimental Results

A. Prototype

Based on the design example in Section V, a 200-W prototype (P_{out} = 100 W and P_{bat} = 100 W) for standard 60-cell PV panels comprising three substrings was built, as shown in Fig. 14. The prototype measures 72×56×16 mm (64.5 cm^3), and its power density is 3.1 W/cm^3. Component values are listed in Table I. The prototype was designed for V_{in} = 28.8 V (typical MPP voltage of 60-cell panels), V_{out} = 28 V, and V_{bat} = 16 V at the switching frequency of 100 kHz.

The measured key operation waveforms at the full load of 200 W are shown in Fig. 15. These waveforms agreed well with the theoretical ones shown in Fig. 7, verifying the operation of the prototype.

B. Output Characteristics

Power conversion efficiencies were measured using the experimental setup shown in Fig. 16. Instead of PV substrings, a constant voltage source with V_{in} = 28.8 V was used as an input voltage source. A variable resistor R_v or an external power supply of V_{ext} = 16 V was connected to the battery port through the selectable tap. Closing the tap X allows I_{bat} to flow toward R_v, emulating the current flow paths in the SIDO mode. To emulate the operation of the SISO mode, the tap X is opened to

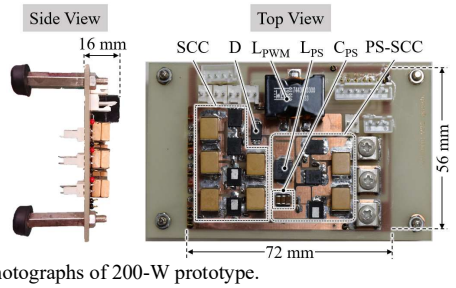

Fig. 14. Photographs of 200-W prototype.

TABLE I
COMPONENT VALUES.

Symbol	Value
Q_1–Q_4, Q_A, Q_B	CSD88599Q5DC, R_{on} = 2.1 mΩ
Q_5, Q_6, Q_C, Q_D	BSC010N04LSI, R_{on} = 1.05 mΩ
C_1–C_5, C_A, C_B	Ceramic capacitor, 100 µF
C_{PS}	Ceramic capacitor, 22 µF × 3
L_{PWM}	33 µH, R_{dc} = 11.40 mΩ
L_{PS}	1.2 µH, R_{dc} = 7.5 mΩ

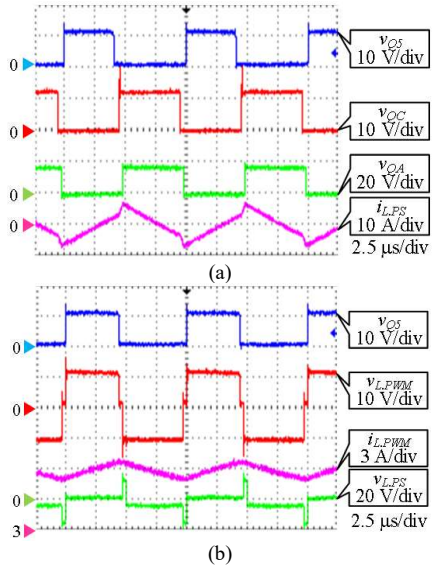

Fig. 15. Measured key waveforms at full load of P_{out} = 100 W and P_{bat} = 100 W. (a) v_{Q5}, v_{QA}, v_{QC}, and i_{LPS}. (b) v_{Q5}, v_{LPWM}, i_{LPWM}, and v_{LPS}.

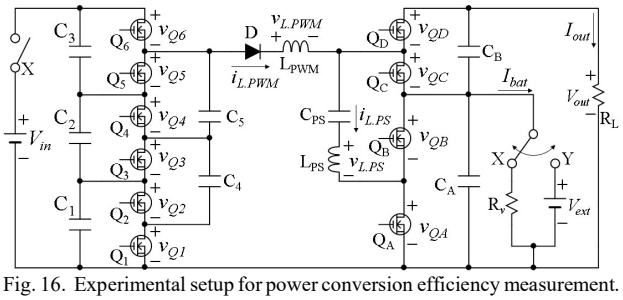

Fig. 16. Experimental setup for power conversion efficiency measurement.

disconnect R_v and V_{in}, while the tap Y is selected to enable V_{ext}.

Power conversion efficiencies in the SIDO mode were measured at fixed P_{out} of 20, 60, and 100 W. Measured efficiencies as a function of the total output power (= $P_{bat} + P_{out}$)

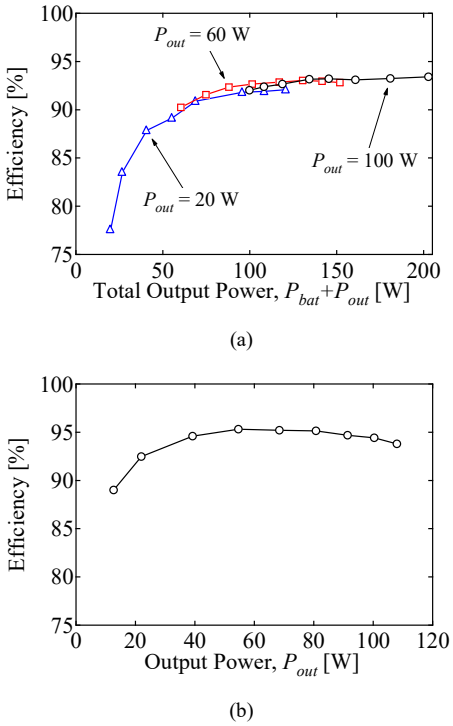

Fig. 17. Measured power conversion efficiencies in (a) SIDO mode and (b) SISO mode.

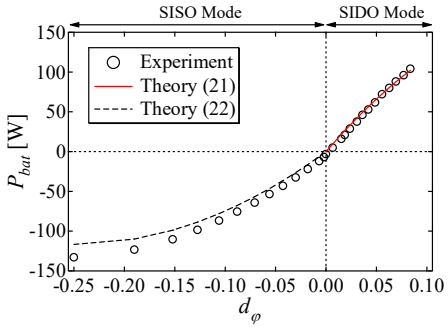

Fig. 18. Measured characteristics of P_{bat} as a function of d_φ.

are shown in Fig. 17(a). The efficiencies increased with P_{out} and were higher than 92% in the range of the total output power greater than 100 W. The peak efficiency was as high as 93.3% at the total output power of 200 W. The measured efficiency in the SISO mode is shown in Fig. 17(b). The efficiency at the rated power of P_{out} = 100 W was as high as 94.4%.

The measured efficiencies of the proposed SCC-MPC in Fig. 17 are somewhat lower than ordinary nonintegrated converters, which generally achieve power conversion efficiencies of 95%–98%. Since the proposed MPC contains ten switches, its gate driving loss will be larger than that of ordinary converters. Furthermore, the SCC-based DPP converter must always operate regardless of the presence of partial shading, whereas a DPP converter in the conventional system [Fig. 2(a)] can be disabled when not necessary. In other words, the loss originating from the SCC impairs power conversion

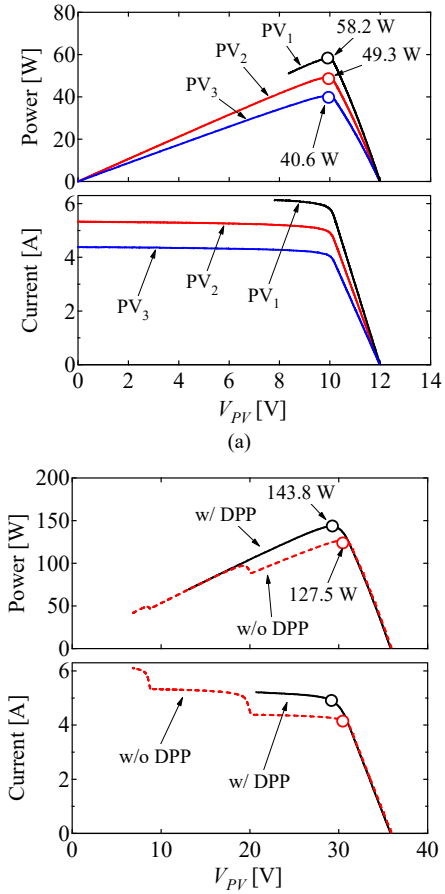

Fig. 19. (a) Individual substring characteristics emulating partial shading condition. (b) *P*–*V* characteristics with/without DPP function.

efficiencies when the DPP function is unnecessary under unshaded conditions.

The measured battery power (P_{bat}) characteristics as a function of d_φ is shown in Fig. 18. The positive and negative regions of P_{bat} correspond to the charging and discharging power, respectively. The experimental results agreed very well with the theoretical characteristics of (21) and (22), verifying the mathematical analysis in Section IV-C. The characteristics in the charging and discharging regions were asymmetric because of the existence of $I_{L.PWM}/2$ in (21) in the charging mode—$I_{L.PWM}$ flows toward the battery in the charging mode, as can be seen in Figs. 8(c)–(e), whereas $I_{L.PWM}$ is blocked by D in the SISO mode.

C. Verification for DPP Capability Under Partial Shading Condition

Solar array simulators (E4361A, Keysight Technologies) were used as substrings to emulate a partial shading condition where PV_2 and PV_3 were moderately and severely shaded, respectively. Individual substring characteristics used for the experiment are shown in Fig. 19(a). Open-circuit voltages of all substrings were set to be 12 V to simplify the experimental setting, though shaded substrings in practical use present lower open-circuit voltages. An electronic load operating in a constant

voltage mode was used as the battery of V_{bat} = 16 V. A variable resistor was connected to the load port to sweep the panel characteristic.

Measured P–V characteristics of the panel with/without the DPP function of the proposed MPC are compared in Fig. 19(b). There were three MPPs observed on the P–V characteristic in the case without the DPP function (i.e., with bypass diodes), and the maximum power at the global MPP was merely 127.5 W. With the DPP function, on the other hand, the local MPP vanished, and the maximum power increased to as high as 143.8 W, achieving 12.8% (= 143.8/127.5 W) improvement in power yield.

D. Mode Transition Tests

Mode transition tests were performed to validate the control system for the proposed MPC. A hill-climbing MPPT algorithm with a duty cycle perturbation of 0.1% and a sampling interval of 200 ms was employed. P_{out} or P_{PV} was step-changed so that P_{bat} swung between the positive and negative values (i.e., charging and discharging).

In the first test, the maximum power of the panel was fixed to be 70 W while P_{out} was step-changed between 50 and 100 W. Measured voltage and power profiles in response to the step changes in P_{out} are shown in Fig. 20(a). The PV panel kept generating 70 W thanks to the MPPT control, and V_{PV} fluctuated at almost three voltage levels [as shown in the inset of Fig. 20(a)]. When P_{out} was 50 W, P_{bat} became positive as the surplus power of P_{PV} was transferred to the battery port. On the other hand, when P_{out} increased to 100 W, the battery port started supplying the deficit power of approximately 30 W. Throughout the test, V_{out} was regulated to be 28 V, though it undershot and overshot to some extent in response to the step changes in P_{out} probably due to insufficient gain turning of the PI controller.

In the second test, P_{out} was fixed to be 100 W while the maximum power of the panel was step-changed between 170 and 0 W. The measured voltage and power profiles in response to the step-change in the panel's maximum power are shown in Fig. 20(b). In the first 40 sec, the MPC operated in the SIDO mode, and V_{out} and V_{bat} were regulated to be 28 and 16 V, respectively. Meanwhile, V_{PV} fluctuated because the input port was unregulated in the SIDO mode. P_{PV} was around 155 W, and the surplus power was delivered to the battery in the form of the positive value of P_{bat}. At 40 sec, P_{PV} was abruptly forced to zero, but the battery port quickly started operating in the SISO mode to support V_{out}. As P_{PV} abruptly rose and exceeded P_{out} at 80 sec, the battery port started being charged again in the SIDO mode as P_{bat} came back to the positive value. In summary, V_{out} was always regulated to be 28 V, though it overshot and undershot to some extent in response to the step changes in P_{PV}. Meanwhile, V_{bat} was regulated to be 16 V during the charging periods.

VIII. Comparison with Conventional MPCs and DPP Converters

The proposed SCC-MPC is compared with conventional nonisolated MPCs in terms of topology, component counts, control schemes, and reported efficiency, as shown in Table II.

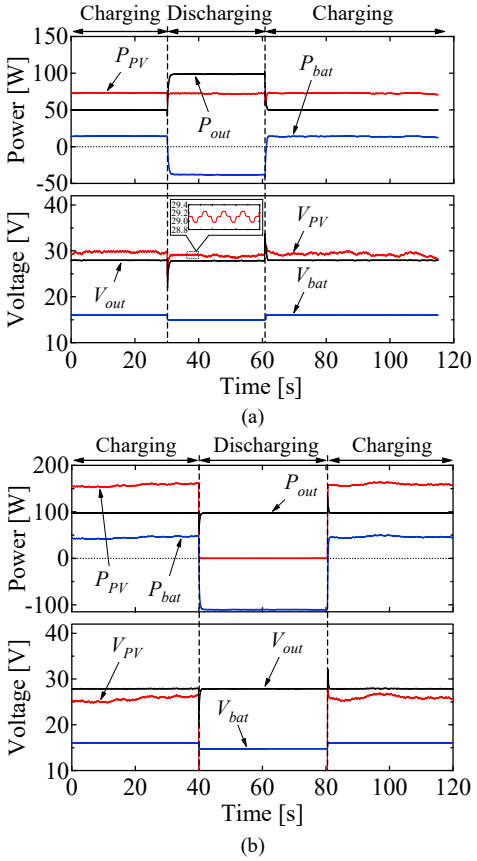

Fig. 20. Measured voltage and power profiles in (a) MPPT mode and (b) SIDO and SISO modes.

Costs are subjectively judged based on the necessary component types and counts.

All topologies have their own unique features and drawbacks. Topologies consisting only of PWM converters [36]–[40] offer a relatively simple circuit. However, since all input/output ports are regulated by PWM controls, duty cycle limitation issues arise. The MPCs [36], [37], for example, manipulate two duty cycles of d_1 and d_2 to control two output ports, but the condition of, e.g., $d_1 > d_2$ must be always satisfied, hence posing the duty cycle limitation. On the other hand, MPCs employing two different modulation schemes ([42]–[44] and proposed MPC) alleviate the duty cycle limitation issues at the cost of increased circuit component counts and increased control complexity. Costs of topologies based on basic PWM converters only [36]–[38] are low, while customized tapped-inductors [40] and the large component count due to the SCC [42] would raise costs.

The proposed SCC-MPC requires the largest component count among the topologies listed in Table II. However, the conventional MPCs integrate only two converters, whereas the proposed converter integrates three converters (i.e., PWM buck-boost converter, PS-SCC, and SCC-based DPP converter), realizing the high integration. Furthermore, the proposed SCC-MPC achieves the miniaturized circuit thanks to the SCC-based structure. Although the proposed SCC-MPC requires a large component count and increases its cost, the highly-integrated

TABLE II
COMPARISON BETWEEN PROPOSED SCC-MPC AND CONVENTIONAL MPCS.

Topology		Component Count				Control Scheme	Full Load Efficiency	Cost	Feature
		Q	D	L	C				
[36], [37]	PWM Converter + PWM Converter	3	0	2	3	PWM + PWM	90% [35] 93% [36]	Low	Simple topology
[38]	Multi-Input/Output PWM Converter	3	3	1	3	PWM + PWM	Not Reported	Low	Single-inductor topology
[39]	PWM Buck-Boost Converter + PWM Buck-Boost Converter	6	0	2	3	PWM + PWM	94%	Medium	Good extendibility
[40]	PWM Converter + PWM Converter	4	5	2 Coupled Inductors	5	PWM + PWM	95%	High	High step-up conversion
[42]	PWM SCC + Series-Resonant Converter	6	4	3	10	PWM + PFM	94%	High	Miniaturized circuit
[43], [44]	PWM Converter + Phase-Shift SCC	4	0	2	4	PWM + Phase-Shift	97.5% [42] 95.7% [43]	Medium	No duty cycle limitation
Proposed	PWM Buck-Boost Converter + Phase-Shift SCC + DPP Converter (SCC)	10	1	2	8	PWM + Phase-Shift	93.3%	High	Miniaturized circuit, high integration

miniaturized circuit is the most prominent feature that would be best suitable for applications where the system miniaturization is prioritized over cost reduction. The efficiency of the proposed SCC-MPC is somewhat inferior chiefly due to the loss originating from the integrated DPP converter, as discussed in Section VII-C—the conventional MPCs in Table II do not contain DPP converters, and therefore losses associated with DPP converter are zero.

The DPP converter in the proposed MPC is based on the SCC. The SCC-based DPP converter and several other representative DPP converter topologies are compared in Table III where n is the number of substrings (e.g., $n = 3$ for standard PV panels consisting of three substrings). Nonisolated bidirectional converters, such as PWM converters [3]−[6] and multi-stage choppers [7], are the most straightforward DPP converter topology, but the existence of multiple inductors is a drawback as magnetics are the bulkiest component in converters. Isolation by bidirectional flyback converters allows flexible power redistribution among substrings [12]−[14]. These DPP converters, however, need numerous transformers in proportion to the number of substrings, increasing the system cost and circuit volume. The single-input−multi-output converters, such as multistacked buck-boost converters [9], [10] and LLC resonant voltage multiplier [11], can reduce the switch count as low as one or two, simplifying their gate driving circuits. However, these DPP converters allow unidirectional power transfer only (from panel to substrings) because of the existence of diodes, and therefore flexible power redistribution is infeasible.

TABLE III
COMPARISON FOR DPP CONVERTERS

Topology	Switch	L	C†	D	Transformer	Feature
Bidirectional PWM Converter [3]–[6]	$2(n-1)$	$n-1$	-	-	-	-
Multi-Stage Chopper [7]	n	$n-1$	-	-	-	-
Bidirectional Flyback Converter [12]–[14]	$2n$	-	-	-	n	Flexible power redistribution
Multistacked Buck-Boost Converter [9], [10]	1	$n+1$	n	n	-	Simple circuit
LLC Resonant Voltage Multiplier [11]	2	-	$n+1$	$2n$	1	Simple circuit
SCC [16] and Proposed	$2n$	-	$n-1$	-	-	High power density

† Smoothing capacitors excluded

Meanwhile, the SCC-based DPP converters [16] essentially do not contain magnetic components, achieving the highest power density among DPP converters listed in Table III, though numerous switches are necessary. In addition, the integration with the PWM buck-boost converter allows to reduce inductor volume because of the inductor's reduced applied voltage, as discussed in Section VI-C.

IX. CONCLUSIONS

To simplify standalone PV systems containing a rechargeable battery and DPP converter, this paper has proposed the novel SCC-based MPC with the DPP capability. The proposed SCC-MPC is derived from the integration of the three converters of a noninverting PWM buck-boost converter, SCC, and PS-SCC, with sharing switches. In addition to the reduced converter count, the proposed MPC achieves reduced circuit volume thanks to the SCC and PS-SCC, both of which are a high power-density converter.

Depending on the power balance among three input/output ports of the PV panel, load, and battery, the proposed SCC-MPC operates either in the SIDO, MPPT, or SISO mode. The output voltage V_{out} is always regulated by PS control adjusting the PS angle φ in any operation scenarios. Duty cycle d_{SCC}, on the other hand, is manipulated based on PWM control to perform either MPPT for the PV panel or CC−CV charging for the battery, depending on the power balance. Meanwhile, partial-shading issues can be automatically precluded by the DPP function of the SCC, even without feedback control.

The experimental verification using the 200-W prototype was performed, and fundamental operations of the proposed MPC were verified. Furthermore, PV panel characteristics with/without the DPP function of the proposed MPC were measured emulating the partial shading condition. With the DPP function, the power yield increased by 12.8%, demonstrating the DPP performance of the proposed MPC. Finally, the power balance test and mode transition test were performed, and the results demonstrated the operation scenarios (MPPT, SIDO, and SISO modes) were seamlessly switched, depending on the power balance among the three input/output ports.

REFERENCES

[1] S.M. MacAlpine, R.W. Erickson, and M.J. Brandemuehl, "Characterization of power optimizer potential to increase energy capture in photovoltaic systems operating under nonuiform conditions," *IEEE Trans. Power Electron*., vol. 28, no. 6, pp. 2936–2945, Jun. 2013.

[2] H. Sato, T. Nakane, and M. Uno, "DPP converter using LLC resonant voltage multiplier with a voltage divider for curved solar roof of PHEVs," in Proc. *IEEE 18th Int. Conf. Power Electron. Motion Control (PEMC)*, pp. 101–1085, Aug. 2018.

[3] H. J. Bergveld, D. Büthker, C. Castello, T. Doorn, A. D. Jong, R. V. Otten, and K. D. Waal, "Module-level dc/dc conversion for photovoltaic systems: the delta-conversion concept," *IEEE Trans. Power Electron*., vol. 28, no. 4, pp. 2005–2013, Apr. 2013.

[4] M.S. Zaman, Y. Wen, R. Fernandes, B. Buter, T. Doorn, M. Dijkstra, H.J. Bergveld, and O. Trescases, "A cell-level differential power processing IC for concentrating-PV systems with bidirectional hysteretic current-mode control and closed-loop frequency regulation," *IEEE Trans. Power Electron*., vol. 30, no. 12, pp. 7230–7244, Dec. 2015.

[5] P.S. Shenoy, K.A. Kim, B.B. Johnson, and P.T. Krein, "Differential power processing for increased energy production and reliability of photovoltaic systems," *IEEE Trans. Power Electron*., vol. 28, no. 6, pp. 2968–2979, Jun. 2013.

[6] S. Qin, C.B. Barth, and R.C.N.P. Podgurski, "Enhancing microinverter energy capture with submodule differential power processing," *IEEE Trans. Power Electron*., vol. 31, no. 5, pp. 3575–3585, May 2016.

[7] T. Shimizu, M. Hirakata, T. Kamezawa, and H. Watanabe, "Generation control circuit for photovoltaic modules," *IEEE Trans. Power Electron*., vol. 16, no. 3, pp. 293–300, May 2001.

[8] J. Du, R. Xu, X. Chen, Y. Li, and J. Wu, "A novel solar panel optimizer with self-compensation for partial shadow condition," in Proc. *IEEE Applied Power Electron. Conf. Expo., APEC*, pp. 92–96, 2013.

[9] M. Uno and A. Kukita, "Single-switch voltage equalizer using multi-stacked buck-boost converters for partially-shaded photovoltaic modules," *IEEE Trans. Power Electron*., vol. 30, no. 6, pp. 3091–3105, Jun. 2015.

[10] M. Uno and A. Kukita, "Current sensorless equalization strategy for a single-switch voltage equalizer using multistacked buck–boost converters for photovoltaic modules under partial shading," *IEEE Trans. Ind. Appl*., vol. 53, no. 1, pp. 420–429, Jan./Feb. 2017.

[11] M. Uno and A. Kukita, "Two-switch voltage equalizer using an LLC resonant inverter and voltage multiplier for partially-shaded series-connected photovoltaic modules," *IEEE Trans. Ind. Appl*., vol. 51, no. 2, pp. 1587–1601, Mar./Apr. 2015.

[12] C. Olalla, C. Deline, D. Clement, Y. Levron, M. Rodríguez, and D. Makisimović, "Performance of power limited differential power processing architectures in mismatched PV systems," *IEEE Trans. Power Electron*., vol. 30, no. 2, pp. 618–631, Feb. 2015.

[13] R. Bell and R.C.N.P. Podgurski, "Decoupled and distributed maximum power point tracking of series-connected photovoltaic submodules using differential power processing," *IEEE J. Emerging Selected Topics in Power Electron*., vol. 3, no. 4, pp. 881–891, Dec. 2015.

[14] G. Chu, H. Wen, L. Jiang, Y. Hu, and X. Li, "Bidirectional flyback based isolated-port submodule differential power processing optimizer for photovoltaic applications," *Solar Energy*, vol. 158, pp. 929–940, Oct. 2017.

[15] Y.T. Jeon, H. Lee, K.A. Kim, and J.H. Park, "Least power point tracking method for photovoltaic differential power processing systems," *IEEE Trans. Power Electron*., vol. 32, no. 3, pp. 1941–1951, Mar. 2017.

[16] J.T. Stauth, M.D. Seeman, and K. Kesarwani, "Resonant switched-capacitor converters for sub-module distributed photovoltaic power management," *IEEE Trans. Power Electron*., vol. 28, no. 3, pp. 1189–1198, Mar. 2013.

[17] A. Blumenfeld, A. Cervera, and M.M. Peretz, "Enhanced differential power processor for PV systems: resonant switched-capacitor gyrator converter with local MPPT," *IEEE J. Emerging Selected Topics Power Electron*., vol. 2, no. 4, pp. 883–892, Dec. 2014.

[18] A.H. Chang, A.T. Avestruz, and S.B. Leeb, "Capacitor-less photovoltaic cell-level power balancing using diffusion charge redistribution," *IEEE Trans. Power Electron*., vol. 30, no. 2, pp. 537–546, Feb. 2015.

[19] M. Uno, Y. Saito, M. Yamamoto, and S. Urabe, "PWM switched capacitor-based cell-level power balancing converter utilizing diffusion capacitance of photovoltaic cells," *IEEE Trans. Power Electron*., vol. 34, no. 11, pp. 10675–10687, Nov. 2019.

[20] M. Uno, M. Yamamoto, H. Sato, and S. Oyama, "Modularized differential power processing architecture based on switched capacitor converter to virtually unify mismatched photovoltaic panel," *IEEE Trans. Power. Electron*., vol. 35, no. 2, pp. 1563–1575, Feb. 2020.

[21] A. Stillwell and R.C.N.P. Podgurski, "A resonant switched-capacitor converter with GaN transistors for high-efficiency power delivery to series-stacked processors," *IEEE JESTPE*, vol. 8. no. 3, pp. 3139–3150, May 2019.

[22] S.R. Sanders, E. Alon, H.P. Le, M.D. Seeman, M. Jhon, and V.W. Ng, "The road to fully integrated dc–dc conversion via the switched-capacitor approach," *IEEE Trans. Power Electron*., vol. 28, no. 9, pp. 4146–4155, Sep. 2013.

[23] M. Uno and A. Kukita, "PWM switched capacitor converter with switched-capacitor-inductor cell for adjustable high step-down voltage conversion," *IEEE Trans. Power Electron*., vol. 34, no. 1, pp. 425–437, Jan. 2019.

[24] J. L. Duarte, M. Hendrix, and M. G. Simoes, "Three-port bidirectional converter for hybrid fuel cell systems," *IEEE Trans. Power Electron.*, vol. 22, no. 2, pp. 480–487, Mar. 2007.

[25] C. Zhao, S. D. Round, and J. W. Kolar, "An isolated three-port bidirectional dc–dc converter with decoupled power flow management," *IEEE Trans. Power Electron.*, vol. 23, no. 5, pp. 2443–2453, Sep. 2008.

[26] H. Krishnaswami and N. Mohan, "Three-port series-resonant dc–dc converter to interface renewable energy sources with bidirectional load and energy storage ports," *IEEE Trans. Power Electron.*, vol. 24, no. 10, pp. 2289–2297, Oct. 2009.

[27] M. C. Mira, Z. Zhang, A. Knott, and M. A. E. Andersen, "Analysis, design, modeling, and control of an interleaved-boost full-bridge three-port converter for hybrid renewable energy systems," *IEEE Trans. Power Electron.*, vol. 32, no. 2, pp. 1138–1155, Feb. 2017.

[28] Y. Hu, W. Xiao, W. Cao, B. Ji, and D. J. Morrow, "Three-port dc–dc converter for stand-alone photovoltaic systems," *IEEE Trans. Power Electron.*, vol. 30, no. 6, pp. 3068–3076, Jun. 2015.

[29] Z. Ding, C. Yang, Z. Zhang, C. Wang, and S. Xie, "A novel soft-switching multiport bidirectional dc–dc converter for hybrid energy storage system," *IEEE Trans. Power Electron.*, vol. 29, no. 4, pp. 1595–1609, Apr. 2014.

[30] J. Zhang, H. Wu, X. Qin, and Y. Xing, "PWM plus secondary-side phase-shift controlled soft-switching full-bridge three-port converter for renewable power systems," *IEEE Trans. Ind. Electron.*, vol. 62, no. 11, pp. 7061–7072, Nov. 2015.

[31] Z. Wang and H. Liu, "An integrated three-port bidirectional dc–dc converter for PV application on a dc distribution system," *IEEE Trans. Power Electron.*, vol. 28, no. 10, pp. 4612–4624, Oct. 2013.

[32] Z. Ding, C. Yang, Z. Zhang, C. Wang, and S. Xie, "A novel soft-Switching multiport bidirectional DC–DC converter for hybrid energy storage system," *IEEE Trans. Power Electron*., vol. 29, no. 4, pp. 1595–1609, Apr. 2014.

[33] J. Deng, H. Wang, and M. Shang, "ZVS three-port DC-DC converter for high-voltage bus-based photovoltaic systems," *IEEE Trans. Power Electron*., vol. 34, no. 11, pp. 10688–10699, Nov. 2019.

[34] X. Sun, Y. Shen, W. Li, and H. Wu, "A PWM and PFM hybrid modulated three-port converter for a standalone PV/battery power system," *IEEE J. Emerging Selected Topics Power Electron*., vol. 3, no. 4, pp. 984–1000, Dec. 2015.

[35] M. Uno, R. Oyama, and K. Sugiyama, "Partially-isolated single-magnetic multi-port converter based on integration of series-resonant converter and bidirectional PWM converter," *IEEE Trans. Power Electron.*, vol. 33, no. 11, pp. 9575–9587, Nov. 2018.

[36] O. Ray, A.P. Josyula, S. Mishra, and A. Joshi, "Integrated dual-output converter," *IEEE Trans. Ind. Electron*., vol. 62, no. 1, pp. 371–382, Jan. 2015.

[37] N. Katayama, S. Tosaka, T. Yamanaka, M. Hayase, K. Dowaki, and S. Kogoshi, "New topology for dc–dc converters used in fuel cell–electric double layer capacitor hybrid power source systems for mobile devices," *IEEE Trans. Ind. Appl.*, vol. 52, no. 1, pp. 313–321, Jan./Feb. 2016.

[38] A.I,S. Senthilkumar, D. Biswas, and M. Kaliamoorthy, "Dynamic power management system employing a single-stage power converter for standalone solar PV applications," *IEEE Trans. Power Electron*., vol. 33, no. 12, pp. 10352–10362, Dec. 2018.

[39] A. Hintz, U. R. Prasanna, and K. Rajashekara, "Novel modular multiple-input bidirectional DC–DC power converter (MIPC) for HEV/FCV application," *IEEE Ind. Electron*., vol. 62, no. 5, pp. 3068–3076, May 2015.

[40] R. Faraji and H. Farzanehfard, "Soft-switched nonisolated high step-up three-port DC–DC converter for hybrid energy systems," *IEEE Trans. Power Electron*., vol. 33, no. 12, pp. 10101–10111, Dec. 2018.

[41] K. Gummi and M. Ferdowsi, "Double-input dc–dc power electronic converters for electric-drive vehicles—topology exploration and synthesis using a single-pole triple-throw switch," *IEEE Trans. Ind. Electron.*, vol. 57, no. 2, pp. 617–623, Feb. 2010.

[42] M. Uno and K. Sugiyama, "Switched capacitor converter based multiport converter integrating bidirectional PWM and series-resonant converters for standalone photovoltaic systems," *IEEE Trans. Power Electron.*, vol. 34, no. 2, pp. 1394–1406, Feb. 2019.

[43] H. Moradisizkoohi, N. Elsayad, and O.A. Mohammed, "A family of three-port three-level converter based on asymmetrical bidirectional half-bridge topology for fuel-cell electric vehicle applications," *IEEE Trans. Power Electron.*, vol. 34, no. 12, pp. 11706–11724, Dec. 2019.

[44] Y. Sato, M. Uno, and H.Nagata, "Nonisolated multiport converters based on integration of PWM converter and phase-shift switched capacitor converter," *IEEE Trans. Power Electron.*, vol. 35, no. 1, pp. 455-470, Jan. 2020.

[45] M. Uno and A. Kukita, "PWM converter integrating switched capacitor converter and series-resonant voltage multiplier as equalizers for photovoltaic modules and series-connected energy storage cells for exploration rovers," *IEEE Trans. Power Electron*., vol. 32, no. 11, pp. 8500–8513, Nov. 2017.

[46] M. Uno and A. Kukita, "Single-switch single-magnetic PWM converter integrating voltage equalizer for partially-shaded photovoltaic modules in standalone applications," *IEEE Trans. Power Electron*., vol. 33, no. 2, pp. 1259–1270, Feb. 2018.

[47] M. Uno and T. Shinohara, "Variable switching frequency modulation scheme for PWM converter integrating series-resonant voltage multiplier-based voltage equalizer for photovoltaic strings under partial shading," *IEEJ Trans. Electrical Electronics Engineering*., vol. 14, no. 3, pp. 467–474, Mar. 2019.

[48] M. Uno and T. Shinohara, "Module-integrated converter based on cascaded quasi-Z-source inverter with differential power processing capability for photovoltaic panels under partial shading," *IEEE Trans. Power Electron*., vol. 34, no. 12, pp. 11553–11565, Dec. 2019.

[49] M. Uno, R. Igarashi, and Y. Sato, "Switched capacitor converter-based PWM plus phase-shift control multiport converter with differential power processing capability for photovoltaic systems," in Proc. *IEEE Int. Conf. Power Electron. (ICPE), ECCE-Asia*, pp. 658–665, May 2019.

[50] Y. Yuanmao, K.W.E. Cheng, and Y.P.B. Yeung, "Zero-current switching switched-capacitor zero-voltage-gap automatic equalization system for series battery string," *IEEE Trans. Power Electron*., vol. 27, no. 7, Jul. 2012, pp. 3234–3242.

[51] M. Uno and K. Tanaka, "Influence of high-frequency charge-discharge cycling induced by cell voltage equalizers on the life performance of lithium-ion cells," *IEEE Trans. Veh. Technol*., vol. 60, no. 4, May 2011, pp. 1505–1515.

[52] M.Y. Kim, C.H. Kim, J.H. Kim, and G.W. Moon, "A chain structure of switched capacitor for improved cell balancing speed of lithium-ion batteries," *IEEE Trans. Ind. Electron*., vol. 61, no. 9, Aug. 2014, pp. 3989–3999.

[53] K. Sano and H. Fujita, "Performance of a high-efficiency switchedcapacitor-based resonant converter with phase-shift control," *IEEE Trans. Power Electron*., vol. 26, no. 2, pp. 344–354, Feb. 2011.

[54] I. Aharon, A. Kuperman, and D. Shmilovitz, "Analysis of dual-carrier modulator for bidirectional noninverting buck–boost converter," *IEEE Trans. Power Electron*., vol. 30, no. 2, pp. 840–848, Feb. 2015.

[55] H. Xiao and S. Xie, "Interleaving double-switch buck–boost converter," *IET. Power Electron*., vol. 5, no. 6, pp. 899–908, May 2012.

[56] J. W. Kimball, P. T. Krein, and K. R. Cahill, "Modeling of capacitor impedance in switching converters," *IEEE Power Electron. Lett*., vol. 3, pp. 136–140, Dec. 2005.

[57] K.A. Kim, P.S. Shenoy, and P.T. Krein, "Converter rating analysis for photovoltaic differential power processing systems," *IEEE Trans. Ind. Electron*., vol. 30, no. 4, pp. 1987–1997, Apr. 2015.

Masatoshi Uno (M'06) was born in Japan in 1979. He received the B.E. degree in electronics engineering and the M.E. degree in electrical engineering from Doshisha University, Kyoto, Japan, and the Ph.D. degree in space and astronautical science from the Graduate University for Advanced Studies, Hayama, Japan, in 2002, 2004, and 2012, respectively.

In 2004, he joined the Japan Aerospace Exploration Agency, Sagamihara, Japan, where he developed spacecraft power systems including battery, photovoltaic, and fuel cell systems. In 2014, he joined the Department of Electrical and Electronics Engineering, Ibaraki University, Ibaraki, Japan, where he is currently an Associate Professor of Electrical Engineering.

His research interests include switching power converters for renewable energy systems, life evaluation for EDLCs and lithium-ion batteries, and development of spacecraft power systems. Dr. Uno received the Isao Takahashi Power Electronics Award in 2018.

Ryuichi Igarashi was born in 1995. He received the B.E. from Tokyo Metropolitan College of Industrial Technology and M.S. degrees in electrical and electronics engineering from Ibaraki University, Ibaraki, Japan in 2018 and 2020, respectively. He is currently with Mitsubishi Electric. His research interests include integrated dc-dc converters renewable energy systems.

Yusuke Sato was born in 1995. He received the B.E. and M.S. degrees in electrical and electronics engineering from Ibaraki University, Ibaraki, Japan in 2017 and 2019, respectively. He is currently with Panasonic corporation. His research interests include dc-dc converters for photovoltaic and energy storage systems.